CHAPTER 3

Structured Materials for Photoelectrochemical Water Splitting

JAMES McKONE AND NATHAN LEWIS*

California Institute of Technology, Division of Chemistry and Chemical Engineering, 1200 E. California Blvd, Pasadena, CA 91125
*Email: nslewis@caltech.edu

3.1 Introduction

Efficient and economical photoelectrochemical water splitting requires innovation on several fronts. Tandem solar absorbers could increase the overall efficiency of a water splitting device, but economic considerations motivate research that employs cheap materials combinations. The need to manage simultaneously light absorption, photogenerated carrier collection, ion transport, catalysis, and gas collection drives efforts toward structuring solar absorber and catalyst materials.

This chapter divides the subject of structured solar materials into two principal sections. The first section investigates the motivations, benefits, and drawbacks of structuring materials for photoelectrochemical water splitting. We introduce the fundamental elements of light absorption, photogenerated carrier collection, photovoltage, electrochemical transport, and catalytic behavior. For each of these elements, we discuss the figures of merit, the critical length scales associated with each process and the way in which these length scales must be balanced for efficient generation of solar fuels. This discussion

RSC Energy and Environment Series No. 9
Photoelectrochemical Water Splitting: Materials, Processes and Architectures
Edited by Hans-Joachim Lewerenz and Laurence Peter

Published by the Royal Society of Chemistry, www.rsc.org

assumes a working knowledge of the fundamentals of semiconductor-liquid junctions; for more details the reader is encouraged to consult review articles.[1–3] The second section of this chapter reviews recent approaches for generating structured semiconductor light absorbers and structured absorber-catalyst composites. This literature review emphasizes the insights gained in the last six years that are specifically related to photoelectrochemical water splitting, rather than to general photoelectrochemistry or photovoltaic applications. This chapter concludes with perspectives and an outlook for future efforts aimed at solar water splitting using structured materials. The realization of a practical, efficient, and useful water splitting device requires significant new developments in materials synthesis as well as deeper understanding of the relevant chemistry and physics. This chapter is intended to motivate such developments.

3.2 Interplay between Materials Properties and Device Characteristics

Practical solar water splitting requires light absorption, separation and collection of photogenerated charge carriers, and charge-carrier transport to catalytic sites to produce gases that must be safely and economically separated and stored. The overall process must occur at economically relevant efficiencies (>10 mA cm^{-2} under 1 sun illumination) with negligible degradation in performance over a multi-year timescale.

One model device for photoelectrochemical water splitting is shown in Figure 3.1. Practical, economical devices may not resemble this model, but it remains useful for highlighting the interplay and design tradeoffs that exist when effectively balancing light management, catalysis, and mass transport. The device in Figure 3.1 utilizes a tandem water-splitting structure in which each solar absorber operates as an electrode for redox chemistry. The use of a tandem solar absorber configuration enables better matching with the solar spectrum,[4,5] and separation of the solar absorber electrodes by embedding each component in a selectively permeable membrane enables the separation of the evolved gaseous products. For solar water splitting, the structured absorber on the top of the device absorbs short wavelength, high-energy photons and transmits longer wavelength photons. This first structured absorber serves as the photoanode, where holes oxidize water to produce oxygen gas and protons with the help of an oxygen-evolving catalyst. At the structured solar absorbing photocathode at the bottom of the device, electrons reduce protons to produce hydrogen gas, assisted by a hydrogen-evolution catalyst. A proton-permeable membrane separates photoanodic oxygen evolution and photocathodic hydrogen evolution to prevent formation of a combustible mixture.

Irrespective of the final device configuration, solar absorbers in photoelectrochemical solar fuels devices must accomplish several tasks. They must convert energetic photons into mobile charge carriers and must facilitate the separation of photogenerated electrons and holes. Either a built-in electric field

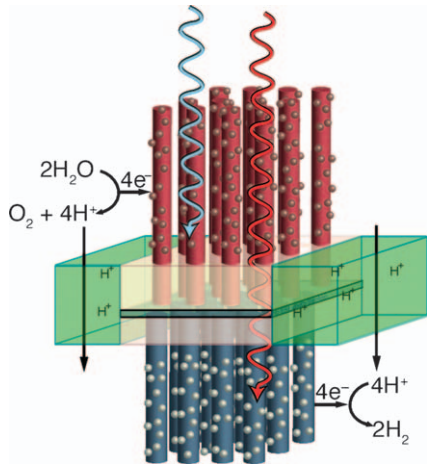

Figure 3.1 Schematic of a proposed water splitting device utilizing tandem, structured solar absorbers and a proton-permeable membrane for ion transport. Image copyright 2013, Elizabeth A. Santori; used with permission.

from a crystalline semiconductor,[3] or kinetic separation as in a dye-sensitized solar cell can accomplish the necessary charge separation.[6] Following charge separation, minority carriers must travel to an interface and perform catalyzed redox chemistry with minimal deleterious carrier recombination. Beyond light absorption and electron/hole collection, the device in Figure 3.1 highlights one of the principal driving forces of structured solar absorbers. In a device that physically separates reduction and oxidation reactions, increasing the distance between the photoelectrodes severely attenuates the device performance due to mass transport effects. A device with structured solar absorber photoelectrodes similar to the configuration in Figure 3.1 offers the potential to reduce performance-attenuating mass transport losses. This chapter discusses several of the aforementioned issues as well as the way in which the structuring of solar absorbers favorably or adversely affects light management, photovoltage, mass transport, and catalysis within a photoelectrochemical cell.

3.2.1 Light Absorption and Collection of Photogenerated Carriers in Crystalline Semiconductors

The nature of the electronic transition that accompanies photon absorption determines the light-absorption properties in semiconductor materials. The requirement for efficient light absorption guides a significant portion of the motivation for structuring solar absorbers, and absorption phenomena contribute to several of the aforementioned figures of merit.

Electronic transitions associated with light absorption in semiconductor materials can be classified according to the alignment of the crystal energy bands with respect to momentum wave vectors in *k*-space.[7] Figure 3.2 highlights this alignment for energy *vs.* crystal momentum diagrams for silicon (left)

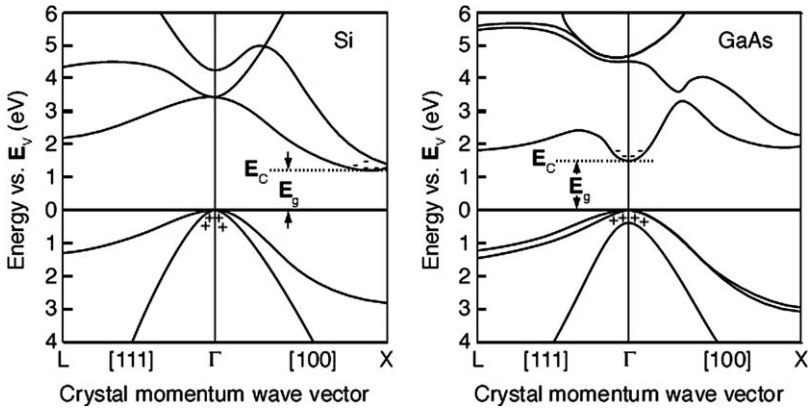

Figure 3.2 Energy versus crystal momentum diagram for the indirect band gap silicon (left) and direct band gap gallium arsenide (right). The differences between the band alignments within these materials yield significantly different photon absorption properties from each other.
Data from Cohen and Chelikowsky.[8]

and gallium arsenide (right).[7,8] For materials such as silicon, in which the maximum of the valence-band energy, $\boldsymbol{E}_v$, and the minimum of the conduction-band energy, $\boldsymbol{E}_c$, do not align, optical absorption requires the absorption or emission of a phonon. Thus silicon has an *indirect* band gap, $\boldsymbol{E}_g$. In contrast to silicon, the conduction band minimum for gallium arsenide is aligned with the valence-band maximum, so photon absorption in GaAs does not require concomitant phonon processes. Gallium arsenide – and all materials with a similar energy *vs*. crystal momentum relationship – have *direct* band gaps.

The nature of the band gap has profound implications for the length scales associated with light absorption. As phonon processes occur on $\sim 10^{-12}$ s timescales, photons must travel significantly longer distances within an indirect band-gap material relative to distances traveled in a direct band-gap material that is limited by the $\sim 10^{-15}$ s timescale for purely electronic interband transitions. Absorption coefficients, α, for direct gap materials are generally much larger than absorption coefficients for indirect-gap materials. As a result, the characteristic absorption length, α^{-1}, is significantly smaller for direct-gap materials relative to α^{-1} for materials with an indirect energy band gap. The plot in Figure 3.3 depicts the differences between α^{-1} for the indirect band-gap material, silicon,[9] relative to α^{-1} for the direct band-gap material, gallium arsenide.[10] For example, at 800 nm, $\alpha_{Si} = 850\ cm^{-1}$, so silicon requires 11.8 μm to absorb 63% (or $1-e^{-1}$) of the incoming light.[9] In contrast, gallium arsenide requires only 1.1 μm to absorb 63% of 800 nm radiation.[10] An understanding of these length scales has profound implications for photoelectrochemistry with semiconductor absorbers.

In a traditional inorganic semiconductor-based photoelectrochemical cell, the collection of photogenerated carriers is linked to the light absorption properties because light absorption and photogenerated minority-carrier collection occur

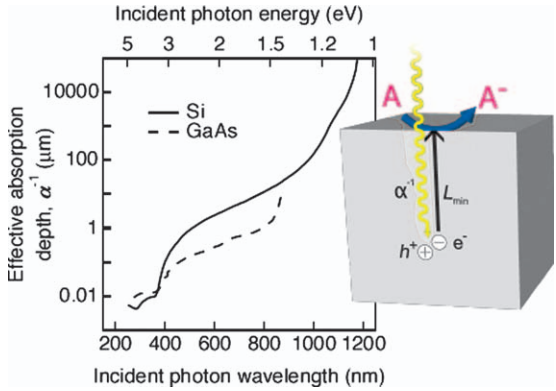

Figure 3.3 The characteristic absorption length, α^{-1}, *vs.* incident photon wavelength for silicon, an indirect absorber material as well as for gallium arsenide, a direct absorber. Over a broad wavelength range, absorption of $1 - e^{-1}$ or 63% of the incoming light requires significantly longer path lengths in silicon relative to gallium arsenide.

along the same spatial axis. Among other factors, efficient carrier collection from bulk crystalline semiconductors requires that the effective minority-carrier diffusion length, L_{min}, is comparable to the penetration depth of the light, α^{-1}. The inset in Figure 3.3 demonstrates the relationship between L_{min} and α^{-1}, which are two critical figures of merit for solar absorbers for photoelectrochemical water splitting. As L_{min} depends on material purity and quality,[11] photoelectrochemical cells that employ this geometry often require highly purified materials, resulting in high overall cost for the active absorber materials. Thus, decoupling L_{min} from α^{-1} is desirable and motivates significant efforts into structured solar absorber materials. The coupling between L_{min} and α^{-1} may not place such a significant restriction on material purity in a direct band-gap solar absorber, but structuring direct band-gap absorbers might still be advantageous for water splitting applications, as discussed in Section 3.2.3.

Long absorption path lengths require highly pure, highly crystalline materials or a modification of light-absorption properties within a semiconductor absorber to achieve optimal performance. Such modifications can reduce the quantity of material required to absorb a significant fraction of above-band-gap photons. In photovoltaic modules, nanoscale interfacial features ideally increase light trapping and decrease the required semiconductor thickness by as much as $4n^2$, where n is the refractive index.[12,13] This enhancement is known as the Lambertian limit, and such nanoscale structuring effectively increases α and decreases α^{-1} but does not fundamentally affect the minority-carrier collection length of the material (techniques for leveraging plasmonic properties for increased light absorption are discussed elsewhere in this volume).

In contrast to increasing light absorption *via* scattering, spatially decoupling light absorption from the collection of photogenerated carriers has the potential to reduce the constraints on purity. Highly-ordered microwire arrays are

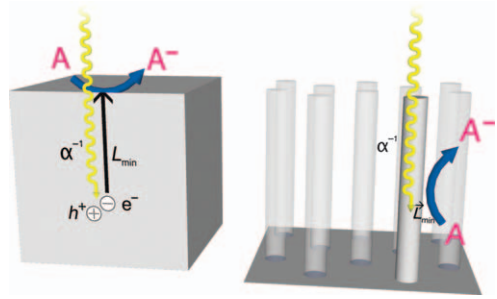

Figure 3.4 Traditional bulk semiconductor geometries (left) require high-quality materials such that the photogenerated minority-carrier diffusion length, L_{min}, is comparable to the characteristic light-absorption length, α^{-1}. In contrast, structured devices such as wire arrays (right) enable the orthogonalization of light absorption and carrier collection. Decoupling L_{min} from α^{-1} reduces certain materials quality constraints.

a prototypical example of a device geometry that decouples light absorption from carrier collection.[14,15] Figure 3.4 contrasts the critical length scales for minority-carrier collection, L_{min}, and α^{-1} for a bulk semiconductor (left) and for a single microwire in a highly ordered array (right). In contrast to the planar, bulk semiconductor case, the microwire-array geometry enables light absorption along the longitudinal wire axis, while photogenerated carrier collection occurs along the radial axis. Thus the microwires can be made sufficiently long for high photon absorption, as implied by Figure 3.3, while maintaining a small radius, permitting the use of semiconductors with low L_{min}. This orthogonalization of light absorption relative to carrier collection is a principal benefit of structured solar absorbers.

In addition to highly ordered microwire arrays, several other structured solar absorber geometries successfully decouple L_{min} from α^{-1}. Section 3.3 of this chapter details recent work on structured absorbers that involve porous morphologies, ordered and un-ordered high-aspect ratio assemblies, and modified dye-sensitized solar cells for photoelectrochemical solar water splitting devices. Each of these geometries presents its own set of benefits and challenges for solar water splitting. However, the remainder of this analysis will focus on highly ordered microwire arrays. We intend this discussion to highlight some of the advantages and disadvantages of structured absorbers and to encourage critical thinking towards nontraditional materials, new geometries, and new characterization techniques for use in photoelectrochemical solar fuels devices.

Experimental, theoretical, and computational modeling studies have indicated that efficient photovoltaic and photoelectrochemical performance can be achieved from highly ordered silicon microwire-array electrodes. This research not only validates the microwire geometry, but also illustrates more generally the benefits provided by structuring solar absorbers. Figure 3.5 presents a summary of light absorption experiments on vapor-liquid-solid (VLS)-grown

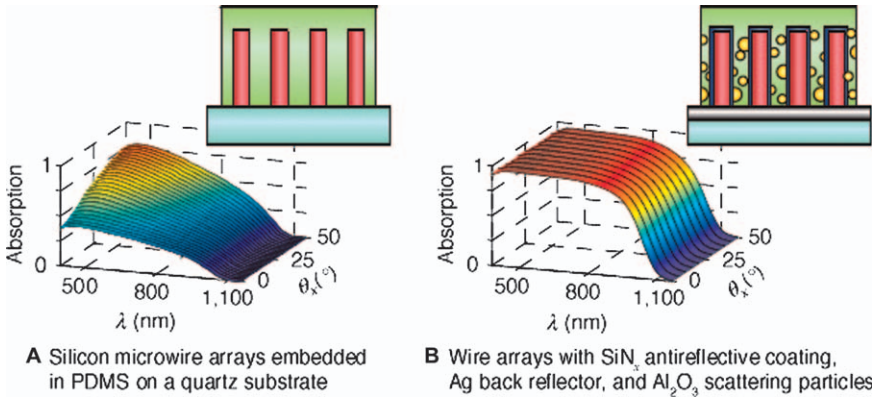

Figure 3.5 Optical absorption results demonstrate that PDMS-embedded silicon microwire arrays have poor absorption at normal incidence but increasing absorption at off-normal angles (frame A). The addition of scattering elements, including a silver back reflector, silicon nitride antireflective coating, and alumina particles, significantly increases absorption at all angles and all wavelengths of incoming light (frame B). Image adapted from Kelzenberg *et al.*[16]

silicon microwire arrays that were impregnated with poly(dimethylsiloxane) (PDMS) and then cleaved from the bulk Si(111) growth substrate. In this configuration, the wire arrays demonstrated poor optical absorbance when illuminated at normal incidence but increasing absorbance as the incoming light was rotated away from the substrate normal (Figure 3.5A).

Light-scattering techniques including a silver back reflector, a silicon nitride antireflective coating, and 900 nm alumina particles embedded in the PDMS each increased the overall light absorption of the microwire arrays. The combination of these three light-trapping methods increased the maximum absorption to 0.96 and increased the normal incidence absorption to 0.92 (Figure 3.5B). The exceptional light-trapping ability of the silicon microwire arrays exceeded the planar light-trapping limit for $\lambda > 800$ nm and also exceeded the simulated day-integrated absorption for planar light-trapping silicon. Interestingly, this light absorption occurred in a structure that had a fractional silicon volume of 4.2%, and a total quantity of silicon equal to a 2.8 μm-thick wafer of identical area. This exceptional light-absorption behavior is a major benefit of structuring solar absorbers.[14,16,17]

In addition to effective light trapping and a reduction in materials purity requirements, structured solar absorbers would not provide viable photovoltaic or photoelectrochemical devices without facilitating effective carrier collection. Several tools for quantifying the carrier properties of bulk semiconductors are also useful for structured solar absorbers. In photoelectrochemical and photovoltaic systems, analyses of the surface recombination velocity, external quantum yield, and internal quantum yield can help elucidate the details of photogenerated carrier transport and recombination within, and at the surface

of, structured semiconductors. Additionally, quantification of the open-circuit photovoltage at an illuminated semiconductor-liquid interface is a primary tool for ascertaining the overall device quality and performance.[18]

3.2.2 Open-Circuit Photovoltage at Structured Semiconductors

Models of charge transfer at illuminated semiconductor-liquid junctions balance the current density of electron-hole pair photogeneration with the current densities for deleterious processes.[1,2,18] Such deleterious currents include carrier recombination in the depletion region, tunneling through the interfacial potential barrier, thermionic emission at the interfacial potential barrier, recombination *via* bulk trap states, recombination *via* surface states, and interfacial charge transfer. Ideally, all of the deleterious currents should be suppressed relative to the current due to carrier recombination in the bulk, which is an intrinsic property of the semiconductor material.[18] Solving the ideal diode equation for zero net current yields equation (3.1), the open–circuit photovoltage, V_{oc}, at illuminated semiconductor-liquid junctions. Since current flow is a kinetic phenomenon, the V_{oc} for an illuminated semiconductor-liquid junction is a kinetic parameter, not a thermodynamic parameter, and represents a fundamental figure of merit for photoelectrochemical water splitting.

$$V_{oc} = \mathrm{n}\frac{k_B T}{q}\ln\frac{J_{ph} N_{D,A} L_{min}}{q D_{min} n_i^2} \tag{3.1}$$

Here n is the diode ideality factor, J_{ph} is the short circuit photocurrent density (photocurrent per area) under illumination, N_D (N_A) is the donor (acceptor) density, L_{min} is the minority-carrier diffusion length, D_{min} is the minority-carrier diffusion coefficient and n_i is the intrinsic carrier density. The term $N_{D,A}^{-1} L_{min}^{-1} q D_{min} n_i^{-2}$ is frequently simplified as J_s, the saturation current density, equation (3.2).

$$V_{oc} = n\frac{k_B T}{q}\ln\frac{J_{ph}}{J_s} \tag{3.2}$$

For bulk, planar semiconductors, the current density ratio on the right hand side of equation 3.2 values reduces to a ratio of the photocurrent to saturation current because the areas in J_{ph} and J_s are identical. However, current density comparisons are more complicated for structured semiconductors. The area defined for photocurrent density refers to the rectilinear parallel projection of the structured semiconductor onto a plane that is illuminated by the incoming light. Such a parallel projection defines the semiconductor projected surface area. Conversely, the area defined for the saturation current density includes the entire contact area of the rectifying junction. For a rectifying junction formed conformally at the interface of a structured semiconductor-liquid junction, the contact area is the geometric surface area of the semiconductor.

The dimensionless figure of merit γ defined in equation (3.3) reconciles the discrepancy between these two areas.[2]

$$\gamma = \frac{\text{geometric surface area}}{\text{projected surface area}} \tag{3.3}$$

Incorporation of γ into equation (3.1) enables a straightforward comparison of the currents and current densities in equation 3.4.

$$V_{oc} = n\frac{k_B T}{q}\ln\frac{J_{ph}}{\gamma J_s} \tag{3.4}$$

Equation (3.4) demonstrates a potential disadvantage of structured solar absorbers. When the semiconductor-liquid junction forms the rectifying contact, increasing the surface area of the solar absorber will decrease the attainable V_{oc} due to the increase in γ. This decrease may be obviated by employing small contact area heterojunctions,[19,20] optical concentrators, or a nanoemitter-style photoelectrochemical cell.[21] The nanoemitter solution could be particularly interesting, as the nanopatterened contact may further function as a scattering element and/or as a solar fuels catalyst. Indeed, the ideally designed nanoemitter solar fuels device may ultimately possess a geometric surface area that is smaller than the projected surface area, yielding $\gamma < 1$ and $V_{oc} > V_{oc,planar}$.

Returning to the example of highly ordered silicon microwire array photoelectrodes, initial studies yielded an open circuit photovoltage, $V_{oc} = 389\,\text{mV}$ and a short-circuit current density, $J_{sc} = 1.43\,\text{mA cm}^{-2}$ for n-Si wire electrodes in contact with dimethylferrocene$^{+/0}$ in methanol under ELH-simulated 1-Sun illumination (halogen lamp).[15] Although this silicon microwire performance was well below the $V_{oc} = 670\,\text{mV}$ and $J_{sc} = 20\,\text{mA cm}^{-2}$ values obtained using planar n-type silicon,[22] these initial studies demonstrated the viability of highly ordered silicon microwire arrays for photoelectrochemistry.

Subsequent experiments on Si microwire arrays established more efficient performance. Spectral response measurements on polymer-embedded, 67 μm-long wire arrays in methyl viologen$^{2+/+\bullet}_{(aq)}$ demonstrated nearly unity internal quantum efficiencies between 400 nm and 900 nm.[17] Scanning photocurrent measurements revealed a minority-carrier effective diffusion length, $L_{eff} = 10\,\mu\text{m}$ in individual 0.9 μm radius silicon microwires,[23] which achieved the $L_{eff} > r$ required to produce efficient photocarrier collection in a microwire configuration.[14] Arrays of p-Si microwires with an n^+ emitter layer achieved $V_{oc} = 540\,\text{mV}$ and energy-conversion efficiencies exceeding 5% for photoelectrochemical hydrogen production under $100\,\text{mW cm}^{-2}$ ELH-simulated 1 Sun illumination using a Pt co-catalyst.[20] These results illustrate the usefulness of the microwire morphology as well as the methodology of employing structured semiconductors for photoelectrochemical water splitting.

Light absorption and photovoltage considerations begin to highlight the complexity involved in designing a highly efficient photoelectrochemical water-splitting device. Next we consider electrochemical transport processes, which incorporate yet another layer of complexity involving larger size scales and are

especially relevant for structured solar absorbers and catalysts for water splitting.

3.2.3 Electrochemical Transport at Structured Semiconductors

The understanding and control of electrochemical transport within a photoelectrochemical cell are critical to the construction of practical solar water-splitting devices. Non-optimized mass transport will result in inefficient use of catalyst material and will also produce overpotentials that degrade the device performance.

Based on comparisons between α^{-1} and L_{min}, indirect-gap semiconductors likely benefit more from structuring than direct-gap semiconductors, because direct absorbers (with larger α values) intrinsically require less material to achieve complete light absorption. However, solar absorbers play roles that are more complicated than converting light to oxidizing and reducing equivalents. In a hydrogen-producing system, balancing the proton flow requires proton-permeable channels between the photoanode and photocathode. The use of two planar, direct-gap semiconductors in the geometry of Figure 3.1 might result in excellent light absorption at the expense of proton flow. Therefore, even direct-gap semiconductors may require a degree of structuring to obtain efficient photoelectrochemical solar fuels devices.

Electrochemical mass transport can be categorized according to three driving forces: convection, migration, and diffusion. Mechanical movement of the bulk solution generates convective transport. Migration refers to the motion of charged species under the influence of electric fields. Concentration gradients produce diffusive transport. A combination of these driving forces determines the mass transport of reactants to an electrode surface and the transport of products away from the electrode surface. Excess supporting electrolyte, or operation in either highly acidic or highly alkaline media, effectively suppresses ion migration forces. Additionally, structured photoelectrodes are likely to suppress bulk solution motion arising from convective forces. Thus, diffusion is likely to dominate mass transport in the vicinity of structured photoelectrodes.

In addition to laminar-flow mass transport phenomena, photoelectrochemical production of gaseous H_2 will affect several aspects of device operation. Gas bubbles will modify light scattering and generate some local solution convection, but it remains unclear whether these factors will produce a net increase or decrease in device performance. Gas bubbles may form at nucleation sites on the photoelectrode surface, decreasing the overall performance by blocking catalytic sites from access to the solution. However, the increased convective flow due to bubble surface detachment and motion may facilitate mass transport.

Mass transport in electrochemical systems has been the focus of significant research for over a century. Such transport studies include mass transport at bulk, planar electrodes,[24] diffusion-limited mass transport during metal deposition at planar microelectrodes,[25,26] and transport near conical and hemispherical ultramicroelectrodes.[27] Several research groups have characterized mass transport, diffusion, and migration phenomena in dye-sensitized solar cells.[28–32] However, mass transport effects at structured solar fuels photoelectrodes remain relatively unexplored.

In contrast to the rigorous mathematical treatments available for planar electrodes and certain microelectrode configurations, models of mass transport do not provide straightforward equations that describe the solution concentration profiles in the vicinity of highly structured electrodes. Recently, simulations in COMSOL Multiphysics have elucidated the mass transport in highly ordered p-type silicon microwire arrays in contact with a solution of cobaltocene$^{+/0}$ in acetonitrile.[33] Figure 3.6 highlights relationships demonstrated by these studies. In simulations where the wire diameter, d, is comparable to the wire pitch spacing, the concentration profile of reactant species resembles a quasi-planar boundary layer (frame A). In contrast, wire array geometries in which $d \ll$ pitch yield a conformal boundary layer (frame B). Simulations that modeled the experimental arrangements demonstrated that the solution-phase reactant concentration decreased to zero over the lower $\sim$70% of the wire length relative to the bulk concentration above the microwire (frame C). In this example, the entire microwire length may be necessary for effective light absorption, but less than one third of the microwire length is an effective redox electrode.

Depletion of solution-phase reactants will adversely affect the photoelectrochemical device performance.[33] A critical adverse effect is a concentration overpotential, η_c, that represents a Nernstian potential shift due to changing concentrations of reactants and products relative to bulk concentrations (equation (3.5)).

$$\eta_c = \frac{RT}{nF}\left(\ln\frac{C_{ox}^{\nu_{ox}}}{C_{red}^{\nu_{red}}} - \ln\frac{C_{ox}^{*\nu_{ox}}}{C_{red}^{*\nu_{red}}}\right) \tag{3.5}$$

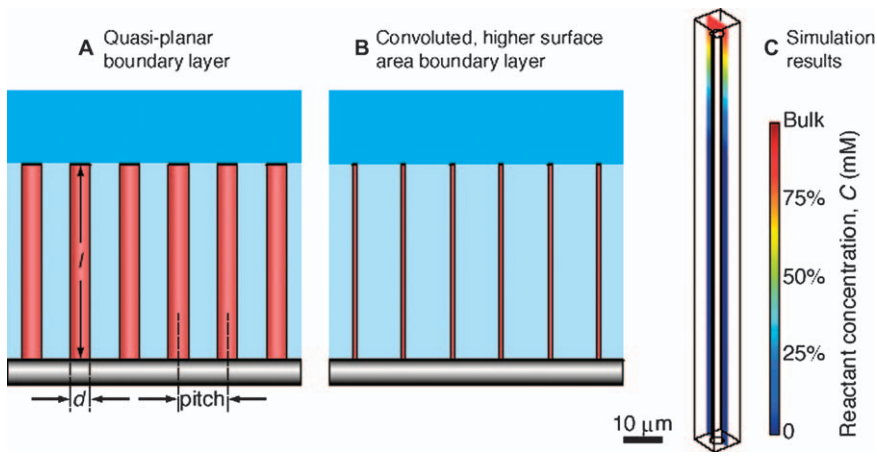

Figure 3.6 The geometries, including size and spacing of solar absorber photoelectrodes, affect solution-phase mass transport. In highly ordered microwire arrays in which the wire diameter is comparable to the spacing, solution phase reactants deplete, forming a quasi-planar boundary layer to the outside solution (frame A). In contrast, the volume between wires is less likely to deplete of reactants when the spacing is significantly greater than the wire diameter (frame B). COMSOL Multiphysics simulation results (frame C) demonstrate the complete depletion of solution-phase reactants over $\sim$70% of the 100 μm wire length.

In equation (3.5), n is the stoichiometric number of electrons transferred, R is the gas constant, F is Faraday's constant C_{Ox} and C_{Red} are the concentrations of oxidized and reduced species at the electrode surface, respectively, C^*_{Ox} and C^*_{Red} are the corresponding concentrations in the bulk solution, and v_{Ox} and v_{Red} are the stoichiometric numbers of the oxidized and reduced species, respectively. This concentration overpotential adds to the kinetic catalyst overpotential that is required to sustain a desired current density from an ideal catalyst, such that $\eta_{total} = \eta_{catalyst} + \eta_c$. Thus, if the surface concentrations or concentration profiles are known, equation (3.5) quantifies the voltage penalty that a structured electrode will incur to overcome mass transport effects associated with its structure.

Simulations that elucidate mass transport effects will be useful when designing and characterizing structured solar absorber photoelectrodes. The characterization of structured photoelectrodes in non-aqueous photoelectrochemical cells with redox species that exhibit facile, 1-electron transfer reactions is also helpful in understanding the interplay between electrode structure and concentration overpotential.

3.2.4 Catalysis at Structured Semiconductors

An understanding of the catalytic phenomena at structured solar absorber materials is not straightforward. In the simple case, a structured solar absorber with a ratio γ of its geometric surface area to its projected surface area should decrease the turnover demands for a conformally deposited catalyst by the same ratio. For example, a highly ordered microwire array containing 100 μm long, 1.8 μm diameter microwires on a 7 μm square pitch exhibits $\gamma = 5.2$. For this microwire array, a catalyst that is uniformly distributed along the structured solar absorber need only support an actual current density of 1.9 mA cm^{-2} for the device to achieve a 10 mA cm^{-2} current density on the basis of projected (i.e. illuminated) area. The implication of this simple case predicts that structuring solar absorbers places a reduced demand on the catalytic rates, and might thus enable the use of non-noble metal catalysts for efficient, economical photoelectrochemical water splitting.

While structured catalysts may indeed reduce the demands for high catalytic activity, several factors complicate the behaviors of structured catalysts. Continuous metallic catalyst layers will behave differently from a discontinuous and/or a non-metallic catalyst. A sufficiently conductive, continuous, metallic catalyst layer deposited on a structured electrode will equilibrate to a uniform potential along the layer surface. Despite being equipotential, this continuous catalyst layer will not necessarily sustain a uniform current density. As Figure 3.6 demonstrates, the volume between adjacent microwires within a highly ordered array quickly depletes of reactants, and the electrode process becomes limited by mass transport from the bulk. Such depletion would render catalyst near the base of the microwire arrays less productive than catalyst material closer to the wire tops. For a non-uniform catalyst layer, all of the catalyst material is not necessarily at an equipotential but rather is at an electrochemical potential that is determined by the minority-carrier

quasi-Fermi level at the local semiconductor-catalyst interface. As a consequence of being poised at different potentials, a non-uniform catalyst layer will result in spatially non-uniform current densities, which may decrease device efficiency.

The catalytic performance is convolved into catalyst structure, photoelectrode structure, light absorption, carrier transport, and mass transport. Challenges will remain for localizing catalyst material in regions along a structured solar absorber to maximize the performance. Similarly, the quantification of catalytic performance and isolation from other processes at structured photoelectrodes will remain a challenge in the development of solar water splitting devices. Structured photoelectrodes, however, will certainly relax the constraints on exchange rates or turnover frequencies.

3.2.5 Outlook

Structuring of solar absorbers offers advantages and disadvantages for a photoelectrochemical solar fuels device. Disadvantages include decreased catalyst utilization efficiency and decreases in open-circuit photovoltage. Advantages include decoupling light absorption and charge-carrier collection, enabling the use of less pure material, and decreasing the turnover constraints on the associated catalyst system. These advantages promise to decrease device costs by permitting use of lower amounts of less pure conventional materials (*e.g.* Si, GaAs, Pt, Ru) or in enabling the use of otherwise less ideal materials (*e.g.* oxide absorbers, non-noble catalysts).

Considering the different optical, carrier generation and mass transport phenomena that occur simultaneously at structured photoelectrodes, it is important to note that very few research groups are incorporating structures and characterizing multiple key phenomena. As this chapter illustrates, photoelectrode structuring is often advantageous to one aspect of overall performance while disadvantageous to another. The most effective studies will therefore combine experimentation and computation to investigate simultaneously several characteristics of a putative photoelectrochemical water-splitting device.

3.3 Review of Recently Demonstrated Advantages of Structured Materials for Photoelectrochemical Water Splitting

This section highlights some features in the development of structured semiconductors and catalysts for the hydrogen evolution reaction (HER), the oxygen evolution reaction (OER), and overall water splitting. We restrict this discussion to developments from the last five years and focus on solar water splitting as opposed to photovoltaics or other photoelectrochemical reactions. Thus, Section 3.3 represents a targeted assessment of the "state of the art" in solar water splitting rather than an exhaustive catalogue of all of the work performed in the field over the last five years.

While research must ultimately investigate solar absorption alongside catalysis, mass transport, and light management, few research groups are addressing the multitude of challenges that exist in the production of a viable photoelectrochemical water splitting device. Therefore, this section presents separately recent experiments and results regarding (1) non-traditional photoelectrode materials with a range of morphologies, (2) the structuring and characterization of traditional semiconductor absorbers, and (3) structured catalyst materials. Finally, this chapter concludes with an outlook and broader considerations for research into practical and efficient photoelectrochemical water splitting.

3.3.1 Metal Oxide Photoelectrodes

Metal oxides have traditionally dominated the field of semiconductor-coupled oxygen evolution, due to the natural stability of the oxides under the highly oxidative conditions demanded by the OER. Accordingly, much recent work has focused on developing highly structured oxides for efficient oxygen evolution.

3.3.1.1 Hematite

Hematite (α-Fe_2O_3), is readily synthesized from inexpensive materials, can be doped n-type, and possesses a 2.2 eV band gap. These properties continue to drive extensive research by several groups. Recent studies have illuminated the fundamental challenge for water oxidation using hematite, namely poor transport properties and short minority-carrier lifetimes resulting in minority-carrier transport distances in the tens of nm.[34,35] Additionally, hematite exhibits strongly anisotropic behavior, with electrons and holes traveling more easily along the (001) crystal planes.[36] All of these difficulties point to the desirability of developing highly nanostructured materials that may permit facile charge carrier collection at the electrolyte interface.

The Grätzel group has successfully achieved control over both the structure and doping of hematite thin films and has demonstrated progressively greater efficiencies for conversion of incident white light to O_2 (g) by synthesizing nanostructured films using both physical and chemical deposition methods. Initial experiments utilized chemical vapor deposition to synthesize hematite films with nanoscale features, producing photocurrent densities of several $mA\,cm^{-2}$ at the thermodynamic water oxidation potential.[37] Subsequent experiments employed solution-phase deposition and generated hematite thin films that achieved similarly large photocurrent densities by decoupling the chemical benefit of sintering from the concomitant increase in feature size.[38]

Several research groups have successfully coupled overlayers on Fe_2O_3 substrates for electronic or catalytic benefits. Zhong and Gamelin electrodeposited a cobalt oxide catalyst onto hematite photoelectrodes and observed enhanced oxygen-evolution activity at potentials less than the thermodynamic oxygen-evolution potential.[39] The Grätzel group noted a similar enhancement in catalytic

activity by deposition of an iridium oxide co-catalyst or through the use of one of several group 13 oxides on the surface of nanostructured Fe_2O_3 films.[40,41]

Another recent area of interest in hematite photoelectrochemistry is the use of plasmonic nanoparticles to enhance light absorption in ultrathin films. Deposition of gold nanoparticles that were tens of nm in diameter increased the light absorption in Fe_2O_3 due to the coupling and scattering of the incoming light with plasmon modes within the nanoparticles.[42,43] Despite the increased light absorption due to plasmonic coupling, Thimsen *et al*. saw no enhancement in water splitting photocurrent.[42] Thomann and coworkers, however, saw an enhancement by more than a factor of ten for photocurrents in the spectral region corresponding to surface plasmon resonances.[43]

Hematite has very promising physical and optical properties, and has garnered much research interest as a water splitting photoanode. However, hematite photoelectrodes have yet to attain sufficient photovoltage (>1 V) or photocurrent density ($>5\,mA\,cm^{-2}$) for efficient water oxidation. Hamann recently provided a thorough discussion of the reasons for the disparity between the expected and actual performance, concluding primarily that methods need to be developed to suppress, or out-compete, charge-carrier recombination at the hematite surface to allow for efficient, productive hole collection.[44]

3.3.1.2 Tungsten Oxide

Tungsten oxide has been the subject of active investigation as a semiconductor for water oxidation. Tungsten oxide does not suffer from the same unfavorable electronic properties as hematite, as in crystalline form it has reasonably long minority carrier lifetimes and isotropic electronic properties. Tungsten oxide is also stable in acidic media. A challenge for WO_3, however, is its indirect band gap of $\sim$2.7 eV, which prevents absorption of a significant fraction of the solar spectrum. Thus, work on nanostructured WO_3 has focused on achieving high quantum efficiencies, on attempts to reduce the band gap, and on the development of nanostructures for more efficient charge capture at the semiconductor-solution interface.

Several recent studies have leveraged the morphology of nanocrystalline WO_3 to maximize light capture and carrier collection. One approach by Hong *et al*. involved the solution phase, hydrothermal synthesis of nanocrystals of WO_3.[45] Calcination at various temperatures afforded control over the grain size of the material. Films that were calcined at 600 °C gave the highest energy-conversion efficiencies, attributable to the best compromise between high crystallinity and high hole collection efficiency.

In another approach, researchers synthesized a unique "flake-wall" morphology in WO_3 nanoparticles that were prepared by a solvothermal method.[46] The technique allowed the deposition of structures directly onto conductive tin-oxide-coated glass plates by seeding with an underlayer of nanocrystalline WO_3. Annealed solvothermal films generated nearly an order of magnitude higher photocurrent densities than un-annealed solvothermal films or the electrodes that had only the nanocrystalline underlayer. In yet another approach,

researchers synthesized WO_3 in a unique inverse opal morphology to enhance light absorption of the films.[47] This inverse-opal structure led to a doubling of photocurrent densities relative to those of conventional, compact films.

Several research groups have also increased the rate of oxygen evolution on WO_3 by the addition of catalysts to the surface of the material. Liu *et al*. used atomic layer deposition (ALD) to deposit an overlayer of Mn oxide on WO_3 and saw a small enhancement in the photocurrent, but a large enhancement of O_2 yield.[48] Seabold and Choi deposited a cobalt oxide catalyst by electrodeposition and observed greatly improved stability for water oxidation on WO_3.[49]

Recently the Lewis group reported that in the absence of catalyst, the faradaic efficiencies of oxygen evolution in acidic media are quite low on WO_3, as oxidation of the electrolyte counter ion (*e.g*. chloride, sulfate, phosphate) is favored over the OER.[50] Catalysts were added either to decompose the oxidized counter ion or to facilitate direct transfer of holes to water molecules, and oxygen evolution proceeded with high faradaic yield.

Given its rather large indirect band gap, WO_3 films will not be viable for efficient photoelectrochemical water splitting unless credible methods can be developed for significantly increasing their visible light absorption without disrupting carrier transport properties. Further details of techniques employed in synthesizing nanostructured and doped WO_3 can be found in a recent review by Liu *et al*.[51]

3.3.1.3 *Bismuth Vanadate*

The optical properties of the monoclinic form of $BiVO_4$ make it similar to, or even more attractive than, WO_3 for driving the OER using visible light irradiation. $BiVO_4$ has a direct band gap of approximately 2.4 eV, allowing efficient absorption of blue photons. Additionally, the band-edge alignment allows generation of a relatively large photovoltage for water oxidation compared to other metal oxides.[52,53]

Several research groups have improved photoelectrochemical water oxidation by the introduction of controlled structure into $BiVO_4$ films. Berglund *et al*. found that deposition of nanostructured, vanadium-rich $BiVO_4$ films resulted in OER activity under illumination that was several times higher than that of stoichiometric films, even after the excess vanadium had dissolved into the electrolyte.[54] Luo *et al*. synthesized $BiVO_4$ films by a chemical bath deposition, resulting in a variety of microstructured morphologies.[55] Interestingly, the highest photocatalytic activities were obtained for films that were relatively compact, although with smaller crystallite size. This result implies that diffusion of holes to the surface may be a limiting factor in the performance of crystalline $BiVO_4$ films.

The photoelectrochemical water oxidation activity of $BiVO_4$ films can also be enhanced by addition of the group VI metals Mo and W. The Bard group carried out a combinatorial study of the Bi-V-W oxide system using a scanning electrochemical microscopy (SECM) technique.[56] They found that a material

consisting of the ratios 4.5 : 5 : 0.5 of Bi, V, and W, respectively, gave the highest photoactivity, both in the combinatorial experiment and in bulk film studies. In another approach, Hong *et al.* synthesized thin film heterojunctions of $BiVO_4$ and WO_3 by sequential deposition of multilayers of the respective precursors.[57] They found that the most active heterojunction consisted of one layer of $BiVO_4$ atop three layers of WO_3. The enhancement was attributed to leveraging of the favorable charge-transfer properties of WO_3 alongside the high light absorption in $BiVO_4$.

Perhaps the most successful approach in the development of $BiVO_4$ photoanodes has been with films that incorporated overlayers of oxide co-catalysts for the OER. The Bard group leveraged their SECM approach to screen combinatorially a variety of catalytic materials deposited onto Bi-W-V oxide films.[58] Interestingly, they found that the highly active OER catalyst iridium oxide did not significantly enhance the photoactivity, whereas the less active catalyst materials Pt and Co_3O_4 did enhance the photocurrent densities by nearly an order of magnitude. They attributed this result to the fact that the interfacial properties of the semiconductor/catalyst junction are critically important in determining overall photoelectrode efficiency.

Several other research groups have found that deposition of oxide catalysts on the surface of $BiVO_4$ photoelectrodes significantly enhances its water oxidation efficiency. Pilli and coworkers observed an enhancement in water oxidation activity for $BiVO_4$ both upon doping with 2% Mo in place of V as well as upon deposition of a cobalt oxide catalyst onto the surface.[59] Zhong *et al.* saw a similar enhancement with a Co oxide co-catalyst on tungsten-substituted $BiVO_4$, which they attributed to efficient suppression of surface recombination on application of the co-catalyst.[60] Seabold and Choi obtained high photocurrent densities (on the order of 2 mA cm^{-2} short-circuit current density) for water oxidation under AM1.5 illumination for a $BiVO_4$ film synthesized by an electrodeposition/calcination technique and coated with an iron oxyhydroxide co-catalyst.[61] These composite films were stable for several hours under oxygen evolution conditions while being illuminated in neutral aqueous electrolytes.

Further efforts are warranted in the suppression of recombination losses in the $BiVO_4$ bulk, as well as coupling efficient OER co-catalysts to the surface for simultaneous enhancement in catalytic activity and suppression of surface recombination losses. Additionally, systematic efforts in the generation of micro- or nanostructured $BiVO_4$ may produce higher charge-carrier collection efficiencies, similar to what has been seen with WO_3 and Fe_2O_3. Also it is important to determine the stability limits of $BiVO_4$ in terms of pH and electrochemical potential in aqueous solutions. With success in these areas, $BiVO_4$ may emerge as a very promising metal oxide photoanode for water oxidation.

3.3.1.4 Other Oxide Systems

Several other systems that are composed of transition metal oxides have gained recent interest for photoelectrochemical water splitting. The Mallouk group

demonstrated a variation on the dye-sensitized solar cell (DSSC) as an oxygen-evolution system.[62] As with a conventional DSSC, the system is comprised of titania nanoparticles that are functionalized with light-absorbing ruthenium bipyridine dyes. Conventional dye-sensitized cells use a reversible redox couple to regenerate the dye from its oxidized state following electron injection into a mesoporous TiO_2 electrode, but the Mallouk system transfers highly oxidizing holes from the dye to an IrO_2 co-catalyst, which then oxidizes water. The electrons injected into the titania layer produce hydrogen at the counter electrode when an additional bias is provided. This type of system allows for utilization of visible photons in oxide-based water-splitting systems, but the overall efficiencies need to be improved. Additionally, the long-term stability of the sensitizer complexes under highly oxidizing conditions needs elucidation.

Several research groups have explored copper (I) oxide (Cu_2O) as a p-type oxide semiconductor material. The Lewis group demonstrated stable photoelectrochemistry, and photovoltages of over 800 mV, from thermally prepared Cu_2O in contact with non-aqueous redox couples.[63] However, stability was lost in aqueous media due to reduction of the oxide to copper metal on the surface, resulting in the subsequent loss of photovoltage. The Grätzel group circumvented the problem of instability of Cu_2O by introducing protective layers of aluminum/zinc oxide and TiO_2 by atomic layer deposition.[64] Their system was able to evolve hydrogen stably for >1 hour using a Pt co-catalyst, albeit with low photovoltages. The Choi group explored the electrodeposition of Cu_2O, and with careful tuning of electrodeposition conditions grew the semiconductor in controllably branched, dendritic structures.[65] Further work on Cu_2O may yield structured materials that can perform the HER efficiently.

3.3.2 High Aspect-Ratio Structures

Over the last decade, significant research efforts have investigated semiconductor nanowires and microwires. The greatest proportion of these efforts has focused on use of wire structures as candidate materials for thin-film photovoltaics and other optoelectronic devices. Several research groups have also developed the wire geometry specifically for photoelectrochemistry and water splitting. The recent review literature contains extensive discussion of the history and progress of nanowire fabrication and solid state devices.[66–72] Here we provide a short overview of the progress on structured Si and III-V semiconductor developments with respect to their potential uses for water splitting.

3.3.2.1 Si Structures

Chemical etching procedures have been developed to generate rods and/or porous structures in silicon in a top-down manner *via* anisotropic metal-assisted etching.[73] A highly porous array of silicon nanowires is produced that has the electronic quality of the parent wafer.[74] This top-down nanostructuring allows for generation of high photocurrent densities, due to the significant

antireflective properties of the etched Si; hence the nickname "black silicon" is given to such nanostructures.[75]

Researchers at the National Renewable Energy Laboratory have successfully used black silicon photocathodes for photoelectrochemical hydrogen generation.[76] Significant enhancements in photocurrent density were observed due to the antireflective properties of the nanoporous coating. Additionally, the onset of hydrogen evolution was shifted positive by several hundred mV for black silicon electrodes relative to planar Si controls. The catalytic shift was attributed to relaxed catalytic turnover requirements as a result of increased Si surface area, and was also likely due to the advantageous presence of trace Au remaining on the porous Si surface after the metal-assisted etching procedure. Chemically-etched silicon nanowire photoelectrochemical solar cells utilizing redox couples other than H^+/H_2 or O_2/H_2O have demonstrated remarkably high solar energy conversion efficiencies,[48,77,78] implying that the water splitting half reactions could also be driven efficiently with the proper electrode architectures and catalysts.

In addition to nanostructures, Si microstructures have also been fabricated by top-down etching procedures, and these systems have been utilized for solar hydrogen generation. Recently, Hou *et al*. demonstrated a photocathode based on p-type Si micropillars that were generated using a dry etching procedure.[79] These pillars were decorated with a molybdenum sulfide cubane cluster as an earth-abundant hydrogen evolution catalyst. The structured composite device generated a photocurrent density of $\sim$10 mA cm^{-2} at the reversible potential for hydrogen-evolution. The observed current density was larger than the photocurrent density generated by a planar control sample. These photocathodes also evolved hydrogen stably for at least one hour.

Silicon nano- and microstructures have also been prepared using a bottom-up synthesis approach that takes advantage of a vapor-liquid-solid growth mechanism, in which a Si/metal eutectic selectively crystallizes silicon onto a substrate from a vapor-phase precursor such as $SiCl_4$ or various silanes.[80] Several research groups have demonstrated VLS-based Si nanowires and microwires in photoelectrochemical solar cells.[15,19,81–84] However, there are only a few examples of VLS-grown silicon structures for photoelectrochemical hydrogen evolution.[20,83] Si microwire arrays can also be embedded in a polymer and removed from the growth substrate while retaining their photoelectrochemical activity,[85–87] potentially allowing fabrication of water-splitting device architectures that utilize tandem solar absorbers on either side of an ionically conductive membrane.[79,88,89]

3.3.2.2 *III-V Structures*

The III-V semiconductors gallium arsenide and indium phosphide have both been utilized as photocathodes for the efficient generation of hydrogen from acidic electrolytes.[90–92] Since both of these materials have direct band gaps, highly structured morphologies might not be needed to improve light absorption or charge-carrier collection. Nevertheless, controlled structuring of the

semiconductor or catalyst layers in III-V photoelectrodes may be desirable to enable novel device geometries or to relax catalyst turnover requirements.

Gallium phosphide is a III-V semiconductor with an indirect fundamental band gap at relatively high energy, making it an interesting candidate as a structured absorber in tandem water-splitting systems. Methods have been devised for top-down formation of wire or porous structures in GaP through anisotropic etching.[93] Recently, the Maldonado group used this electrochemical etching technique to generate nanostructured n-type and p-type gallium phosphide with vertically oriented pores of varying depth.[94,95] The structured material showed much greater efficiency than planar controls for collecting excited charge carriers in both regenerative and fuel-forming modes.

Thus far, oxygen or hydrogen evolution has not been reported from highly structured III-V semiconductors. This is due in part to the low stability of III-V semiconductors under the reducing or oxidizing conditions required for the HER and OER, respectively. An illustrative example is the work of Khasalev and Turner on a full water-splitting system based on multi-junction, planar, III-V semiconductors.[96] Although this system generated hydrogen and oxygen with high energy-conversion efficiency, it was stable for only a few hours. With continued progress in nanoscale control over composition and morphology, water-splitting devices based on III-V semiconductors might be made stable under long-term operation.

3.3.3 Water Splitting by Colloidal Particles

Many research groups have attempted to split water using colloidal particles. A recent analysis has suggested that colloidal water splitting is the best approach for efficient, scalable solar hydrogen generation, provided that the colloidal species are composed of abundant elements and provided that that inexpensive and safe methods for separating the products from an explosive mixture can be developed.[97]

To date, there are very few examples of full water splitting that use colloidal particle suspensions in the absence of sacrificial reagents. The Domen group has reported the net generation of H_2 and O_2 gases in colloidal systems through careful suppression of the parasitic (and thermodynamically downhill) back-reactions.[98,99] The researchers relied on an overlayer of CrO_3 on Rh particles deposited onto colloidal particles of GaN/ZnO solid solutions. The chromia overlayer enabled net water splitting on these particles by affording selectivity of the Rh cores for the HER, due to selective permeability of CrO_3 to protons and H_2 but not water or oxygen. Work from the Domen group is detailed elsewhere in this volume, but this selective system is worth noting for its control over nanostructure, providing the necessary components for overall water splitting.

3.3.4 Water Splitting Catalysis by Structured Materials

Several research groups have advanced the development of nanostructured catalysts for the HER and the OER. Significant work has focused on the

replacement of the noble metals Pt, Ru, and Ir that are commonly used in proton-exchange membrane electrolyzers, with non-noble alternatives, or on leveraging structured geometries to minimize the quantities of expensive elements. The following is a brief discussion of several research highlights in the development of heterogeneous HER and OER catalysts, with special emphasis on systems that have been developed with control of features at the nanoscale.

3.3.4.1 *Hydrogen Evolution*

Several research groups have recently demonstrated molybdenum sulfides as catalysts for the HER.[100] These sulfides have been widely studied for their use in hydrodesulfurization,[101] but have demonstrated viability as hydrogen-evolution catalysts based on DFT calculations from the Nørskov group that suggested the HER catalytic activity of such systems could approach that of pure Pt.[102] Subsequent experimental work in the Chorkendorff group demonstrated facile HER catalysis at the edge sites of nanocrystalline MoS_2 lamellae.[103]

Recent work from the Chorkendorff and Jaramillo groups sought to maximize the density of active edge sites of MoS_2. For example, a precursor was deposited onto high surface-area carbon paper and subsequently annealed under a sulfidizing atmosphere to yield a supported catalyst of nominally high surface area.[104] This carbon-supported metal sulfide catalyst produced exchange current densities on the order of 10^{-6} A cm^{-2} based on estimated total surface area. The activity was increased by addition of small amounts of Co salts to the precursor solutions. The Jaramillo group reported catalytic activity from a structured MoO_3-MoS_2 core-shell morphology.[47] Synthesized by sulfidizing the outer layer of a nanostructured MoO_3 layer, this morphology avoided ohmic losses due to high resistivity of the MoS_2, which is far less conductive than MoO_3. The high surface area MoO_3-MoS_2 composite attained high geometric activity and demonstrated extended stability under acidic conditions.

Transition metal sulfide electrocatalysts can be deposited from molecular precursors onto structured Si for photoelectrochemical hydrogen evolution. As discussed previously, Hou *et al*. observed efficient catalysis to yield a net energy conversion of incoming light energy to stored energy in H_2(g).[79] A subsequent systematic study of transition metal sulfides derived from molecular precursors observed the highest energy conversion efficiency from Mo and Cu/Mo sulfides, but the highest stability was exhibited by pure Mo sulfide.[105]

Amorphous, rather than crystalline, molybdenum sulfide also is an efficient HER catalyst. This active material can be either electrodeposited from ammonium thiomolybdate under anaerobic conditions or can be chemically synthesized by precipitation of nanoparticles.[106,107] Interestingly, the electrodeposited material is formed by passing both anodic and cathodic current through the working electrode, which is unusual for a material intended only to catalyze a reduction reaction. Similar to the results of Chorkendorff *et al*.,

Merki *et al.* observed an enhancement in activity upon the addition of the first row metals Fe, Ni, and Co to the amorphous films.[107]

Several groups have characterized the catalytic activity of molybdenum-containing alloys. Rocheleau *et al.* studied a Co-Mo catalyst for solar water splitting,[108] and the Lewis group studied a Ni-Mo alloy for photoelectrochemical hydrogen evolution.[83] Previously studied for alkaline electrolyzer applications, Ni-Mo has demonstrated high activity over thousands of hours.[109,110] Lewis and coworkers showed that an alloy of Ni and Mo could be electrodeposited directly onto p-type Si substrates for efficient hydrogen evolution under mildly acidic conditions. The as-deposited films were nanoparticulate, and the apparent catalytic activity increased when the material was deposited onto Si microwire arrays, due to the multi-scale roughness enhancement afforded by the nanostructured catalyst on the microstructured semiconductor substrate. Researchers at Sun Catalytix have recently employed a related catalyst system, Ni-Mo-Zn, which was integrated into a water splitting cell that utilized a triple junction amorphous silicon solar cell as a substrate.[111] Three-component Ni-Mo-X catalysts have been previously studied for alkaline electrolysis,[112,113] whereas the Sun Catalytix researchers reported stable performance under buffered conditions at neutral pH.

3.3.4.2 Oxygen Evolution

Significant recent efforts have targeted understanding and development of cobalt oxide for the OER. The 2008 publication by Kanan and Nocera stimulated recent investigations into cobalt oxide catalysts in which amorphous Co oxide is electrodeposited at neutral pH from Co salts.[114] These recent studies follow from previous research on Co oxides for water oxidation in alkaline and neutral pH.[115–117] The initial experiments suggested that the phosphate buffer played some role in the formation of the catalyst, although subsequent work has shown that other buffers, or Co metal films, generate similar coatings.[118,119]

The reports on Co oxide catalysts have driven efforts to understand the mechanism of their operation. Nocera and coworkers utilized EPR and X-ray techniques to suggest a cubane structure for the active species, where the Co is proposed to undergo a redox transition from Co^{III} to Co^{IV} during catalytic turnover.[120] Studies of Co oxide OER catalysts over a range of pH suggest that the active catalytic mechanism transitions from primarily heterogeneous to primarily homogeneous at pH values below 3.[121]

The Nocera group has investigated Co oxide as a commercially viable system for efficient solar driven oxygen evolution. They generated current densities of tens of mA cm^{-2} for oxygen evolution at overpotentials below 300 mV in neutral pH at amorphous Co oxide deposited onto high surface area Ni foams.[122] Additionally, this electrodeposited Co oxide catalyst resisted poisoning by Ca^{2+} ions and other contaminants found in natural waters, and the catalyst exhibited a linear increase in catalytic activity with mass loading. This linear scaling of activity with mass loading implies that the electrodeposited Co oxide catalyst exhibits a large electrochemically active surface area for the

OER, either as a result of nanoscale features or due to three-dimensional porosity in the film. The same methodology for the deposition of Co oxide films has been used in several functional systems for solar water splitting incorporating amorphous and crystalline Si semiconductors.[111,123,124]

Several researchers have incorporated Co oxide catalysts as active materials for driving the OER on semiconductor absorber substrates. The Gamelin group deposited amorphous Co oxide onto nanocrystalline hematite, yielding an increase in the overall efficiency for oxygen evolution.[39,125] The Choi group deposited Co oxide onto ZnO and hematite nanostructures under illumination and found that the catalyst morphology and energy-conversion efficiency could be modulated by judicious control of the deposition conditions.[126,127] The Choi group also deposited Co oxide onto WO_3 photoelectrodes and observed a significant increase in the selectivity of the composite film toward oxygen evolution relative to formation of peroxo-species, which also enhanced the long-term stability of the oxygen-evolution system.[49]

In addition to studies of non-noble metal catalysts, a traditional water oxidation catalyst, IrO_2, is of interest with the goal of minimizing the iridium loading while maintaining high oxygen evolution activity. The Murray group reported a mesoporous IrO_2 film consisted of nanoscale oxide particles that were synthesized in the solution phase and then flocculated onto an electrode that was maintained at positive bias.[128] Significant oxygen-evolution activity with 100% Faradaic efficiency was observed at overpotentials as low as 250 mV. Additionally, the Mallouk group has published several deposition methods that produce nanoscale iridium oxide films for electrochemical oxygen evolution.[129]

Nanoscale noble metals and oxides have recently been explored for both of the water splitting half reactions on planar Si electrodes that are protected from deleterious interfacial reactions by thin oxide layers. Lewerenz and Muñoz have carried out extensive work on so-called ''nanoemitter'' junctions between planar Si and either Pt or Ir metals accompanied by surface Si oxide. They demonstrated stable, sustained electrochemical reactions on Si surfaces under conditions that normally result in silicon degradation.[130] McIntyre, Chidsey, and coworkers recently leveraged ALD-deposited TiO_2 for the protection of planar n-type Si electrodes for sustained oxygen evolution under alkaline conditions using an evaporated Ir co-catalyst.[131]

3.3.5 Advances in Modeling Heterogeneous Catalysis

Computational modeling of active redox catalysis for the water-splitting half reactions has produced notable, recent advances. Several research groups, led primarily by Nørskov and collaborators, have recently undertaken the challenge of developing DFT models that are sufficiently accurate to *predict* active materials for the efficient evolution of hydrogen and oxygen, as well as other fuel-forming reactions.[132,133]

Recent DFT modeling studies indicate a need for nanoscale control over the catalyst composition and morphology. Nørskov *et al.* predicted that the

activity of MoS_2 for hydrogen evolution would stem primarily from active sites at the edges of the lamellar crystal structure.[102] This prediction was confirmed experimentally by the Chorkendorff lab.[103] These results imply that molybdenum sulfides must be nanostructured to maximize the proportion of step edge sites and thus obtain an optimum hydrogen evolution efficiency.

Other recent work showed that composites consisting of adlayers of one metal on another could attain higher catalytic activities for the HER than either of the constituent metals.[134,135] These results suggest that new structural/compositional motifs can be used for new, highly catalytic nanomaterials to be coupled with light absorbers for efficient water splitting.

DFT modeling results from Nørskov and Rossmeisl indicate conserved differences in energy between intermediates for the OER on transition metal oxides.[136,137] These relationships may result in an upper bound for the catalytic activity of any metal oxide OER catalyst that is modest in comparison with the high activities of noble metals for hydrogen evolution. The development of multifunctional catalysts that consist of chemically distinct "active sites" for various primary steps could circumvent this limitation. These sites would need to be located sufficiently closely to allow facile exchange of intermediate species, and would thus require control over composition and structure at the nanoscale. With several applications beyond photoelectrochemical water splitting, the successful demonstration of a rationally designed nanoscale, multifunctional electrocatalyst would be very significant.

3.3.6 Broader Considerations – Beyond Small

Recent efforts in the development of systems for photoelectrochemical water splitting demonstrate the need for control over composition and morphology at the micro, nano, and even atomic scale. In addition, successful photoelectrochemical water splitting systems based on nanostructured film morphologies require a proper understanding of mass transport in relation to nanostructured geometries. Alternatively, colloidal water-splitting systems may require some form of convection to maintain particles in the suspended form. Both of these characteristics demand an understanding of diffusion and convection of species from the nanoscale to the tens or hundreds of micron scale. Efficient generation of O_2 and H_2 gas implies copious bubble formation, the dynamics of which may significantly influence key characteristics such as light absorption and reactant transport. New work must address all such features of an overall water splitting process.

The potential need for gas separation and pressure management in water splitting systems also requires study. Systems with no physical barrier between the oxygen-evolving anode and the hydrogen-evolving cathode may require a means to minimize losses from the comparatively facile reverse reactions of oxygen reduction and hydrogen oxidation, respectively. Barrierless systems will also require schemes to safely manage and separate an explosive H_2/O_2 mixture. Systems that employ a separator between the anode and cathode must minimize ohmic losses due to ionic transport over distances between the two

compartments. Another key concern for multi-compartment systems is the potential need for active pressure management, as the 2:1 stoichiometry of hydrogen and oxygen evolution, respectively, implies rapid buildup of differential pressures that may affect sustained operation of the system.

Many key insights involving distance scales larger than a few microns can be gained from previous experience as well as from collaborations between the fields of chemical engineering and systems design. If we are to have economical solar water splitting systems in the near future, both large scale and small scale developments must continually feed back to one another to efficiently move toward functional, scalable solutions.

Acknowledgements

This work was supported in part by the Joint Center for Artificial Photosynthesis, a DOE Energy Innovation Hub. The contribution from NSL was supported through the Office of Science of the U.S. Department of Energy under award No. DE-SC0004993; the contributions from JRM and RLG were supported by BP and by the U.S. Department of Energy under award No. DE-FG02-03ER15483. JRM additionally acknowledges the U.S. Department of Energy Office of Science for a graduate research fellowship.

References

1. M. X. Tan, P. E. Laibinis, S. T. Nguyen, J. M. Kesselman, C. E. Stanton and N. S. Lewis, *Prog. Inorg. Chem.*, 1994, **41**, 21–144.
2. M. G. Walter, E. L. Warren, J. R. McKone, S. W. Boettcher, Q. X. Mi, E. A. Santori and N. S. Lewis, *Chem. Rev.*, 2010, **110**, 6446–6473.
3. S. Maldonado, A. G. Fitch and N. S. Lewis, in *Nanostructured and photoelectrochemical systems for solar photon conversion*, ed. M. D. Archer and A. J. Nozik, Imperial College Press, London, 2008, vol. 3.
4. J. R. Bolton, S. J. Strickler and J. S. Connolly, *Nature*, 1985, **316**, 495–500.
5. A. J. Bard and M. A. Fox, *Acc. Chem. Res.*, 1995, **28**, 141–145.
6. M. Grätzel and J. R. Durrant, in *Nanostructured and photoelectrochemical systems for solar photon conversion*, ed. M. D. Archer and A. J. Nozik, Imperial College Press, London, 2008, vol. 3.
7. S. M. Sze and K. K. Ng, *Physics of Semiconductor Devices*, 3rd edn., Wiley-Interscience, New York, 2007.
8. M. L. Cohen and J. R. Chelikowsky, *Electronic structure and optical properties of semiconductors*, 2nd edn., Springer-Verlag, Berlin, 1988.
9. M. A. Green and M. J. Keevers, *Prog. Photovoltaics*, 1995, **3**, 189–192.
10. H. C. Casey, D. D. Sell and K. W. Wecht, *J. Appl. Phys.*, 1975, **46**, 250–257.
11. V. Schlosser, *IEEE Trans. Electron Dev.*, 1984, **31**, 610–613.
12. S. E. Han and G. Chen, *Nano Lett.*, 2010, **10**, 4692–4696.
13. E. Yablonovitch, *J. Opt. Soc. Am.*, 1982, **72**, 899–907.

14. B. M. Kayes, H. A. Atwater and N. S. Lewis, *J. Appl. Phys.*, 2005, **97**, 114302.
15. J. R. Maiolo, B. M. Kayes, M. A. Filler, M. C. Putnam, M. D. Kelzenberg, H. A. Atwater and N. S. Lewis, *J. Am. Chem. Soc.*, 2007, **129**, 12346–12347.
16. M. D. Kelzenberg, S. W. Boettcher, J. A. Petykiewicz, D. B. Turner-Evans, M. C. Putnam, E. L. Warren, J. M. Spurgeon, R. M. Briggs, N. S. Lewis and H. A. Atwater, *Nature Mater.*, 2010, **9**, 239–244.
17. M. D. Kelzenberg, PhD thesis, California Institute of Technology, 2010.
18. N. S. Lewis, *J. Electrochem. Soc.*, 1984, **131**, 2496–2503.
19. S. W. Boettcher, J. M. Spurgeon, M. C. Putnam, E. L. Warren, D. B. Turner-Evans, M. D. Kelzenberg, J. R. Maiolo, H. A. Atwater and N. S. Lewis, *Science*, 2010, **327**, 185–187.
20. S. W. Boettcher, E. L. Warren, M. C. Putnam, E. A. Santori, D. Turner-Evans, M. D. Kelzenberg, M. G. Walter, J. R. McKone, B. S. Brunschwig, H. A. Atwater and N. S. Lewis, *J. Am. Chem. Soc.*, 2011, **133**, 1216–1219.
21. T. Stempel, M. Aggour, K. Skorupska, A. Munoz and H. J. Lewerenz, *Electrochem. Commun.*, 2008, **10**, 1184–1186.
22. M. L. Rosenbluth and N. S. Lewis, *J. Am. Chem. Soc.*, 1986, **108**, 4689–4695.
23. M. C. Putnam, D. B. Turner-Evans, M. D. Kelzenberg, S. W. Boettcher, N. S. Lewis and H. A. Atwater, *Appl. Phys. Lett.*, 2009, **95**.
24. A. J. Bard and L. R. Faulkner, *Electrochemical Methods: Fundamentals and Applications*, 2nd. edn., Wiley, New York, 2001.
25. B. Scharifker and G. Hills, *J. Electroanal. Chem.*, 1981, **130**, 81–97.
26. J. Mostany, J. Mozota and B. R. Scharifker, *J. Electroanal. Chem.*, 1984, **177**, 25–37.
27. R. M. Penner, M. J. Heben and N. S. Lewis, *Anal. Chem.*, 1989, **61**, 1630–1636.
28. G. P. Kalaignan and Y. S. Kang, *J. Photoch. Photobio. C*, 2006, **7**, 17–22.
29. Y. Lin, Y. T. Ma, L. Yang, X. R. Xiao, X. W. Zhou and X. P. Li, *J. Electroanal. Chem.*, 2006, **588**, 51–58.
30. W. Hyk and J. Augustynski, *J. Electrochem. Soc.*, 2006, **153**, A2326–A2341.
31. N. Papageorgiou, M. Gratzel and P. P. Infelta, *Sol. Energ. Mat. Sol. C*, 1996, **44**, 405–438.
32. J. J. Lee, G. M. Coia and N. S. Lewis, *J. Phys. Chem. B*, 2004, **108**, 5269–5281.
33. C. Xiang, A. C. Meng and N. S. Lewis, *Proc. Natl. Acad. Sci. USA*, 2012, **109**, 15622–15627.
34. B. M. Klahr and T. W. Hamann, *J. Phys. Chem. C.*, 2011, **115**, 8393–8399.
35. K. Sivula, F. Le Formal and M. Grätzel, *ChemSusChem*, 2011, **4**, 432–449.
36. C. M. Eggleston, A. J. A. Shankle, A. J. Moyer, I. Cesar and M. Grätzel, *Aquat. Sci.*, 2009, **71**, 151–159.

37. A. Kay, I. Cesar and M. Gratzel, *J. Am. Chem. Soc.*, 2006, **128**, 15714–15721.
38. J. Brillet, M. Gra, K. Sivula and P. Fe, *Nano Lett.*, 2010, **10**, 4155–4160.
39. D. K. Zhong and D. R. Gamelin, *J. Am. Chem. Soc.*, 2010, **132**, 4202–4207.
40. T. Hisatomi, F. Le Formal, M. Cornuz, J. Brillet, N. Tétreault, K. Sivula and M. Grätzel, *Energy Environ. Sci.*, 2011, **4**, 2512–2515.
41. S. D. Tilley, M. Cornuz, K. Sivula and M. Grätzel, *Angew. Chem., Int. Ed.*, 2010, **122**, 6549–6552.
42. E. Thimsen, F. Le Formal, M. Grätzel and S. C. Warren, *Nano Lett.*, 2011, **11**, 35–43.
43. I. Thomann, B. A. Pinaud, Z. Chen, B. M. Clemens, T. F. Jaramillo and M. L. Brongersma, *Nano Lett.*, 2011, **11**, 3440–3446.
44. T. W. Hamann, *Dalton Trans.*, 2012, **41**, 7830–7834.
45. S. J. Hong, H. Jun, P. H. Borse and J. S. Lee, *Int. J. Hydrogen Energy*, 2009, **34**, 3234–3242.
46. F. Amano, D. Li and B. Ohtani, *Chem. Commun. (Cambridge, U.K.)*, 2010, **46**, 2769–2771.
47. X. Chen, J. Ye, S. Ouyang, T. Kako, Z. Li and Z. Zou, *ACS Nano*, 2011, **5**, 4310–4318.
48. R. Liu, Y. Lin, L.-Y. Chou, S. W. Sheehan, W. He, F. Zhang, H. J. M. Hou and D. Wang, *Angew. Chem., Int. Ed.*, 2011, **50**, 499–502.
49. J. A. Seabold and K.-S. Choi, *Chem. Mater.*, 2011, **23**, 1105–1112.
50. Q. Mi, A. Zhanaidarova, B. S. Brunschwig, H. B. Gray and N. S. Lewis, *Energy Environ. Sci*, 2012, **5**, 5694–5694.
51. X. Liu, F. Wang and Q. Wang, *Phys. Chem. Chem. Phys.*, 2012, **14**, 7894–7911.
52. K. Sayama, A. Nomura, T. Arai, T. Sugita, R. Abe, M. Yanagida, T. Oi, Y. Iwasaki, Y. Abe and H. Sugihara, *J. Phys. Chem. B*, 2006, **110**, 11352–11360.
53. A. Walsh, Y. Yan, M. N. Huda, M. M. Al-jassim and S.-H. Wei, *Chem. Mater.*, 2009, **21**, 547–551.
54. S. P. Berglund, D. W. Flaherty, N. T. Hahn, A. J. Bard and C. B. Mullins, *J. Phys. Chem. C.*, 2011, **115**, 3794–3802.
55. W. Luo, Z. Wang, L. Wan, Z. Li, T. Yu and Z. Zou, *J. Phys. D: Appl. Phys.*, 2010, **43**, 405402–405402.
56. H. Ye, J. Lee, J. S. Jang and A. J. Bard, *J. Phys. Chem. C*, 2010, **114**, 13322–13328.
57. S. J. Hong, S. Lee, J. S. Jang and J. S. Lee, *Energy Environ. Sci.*, 2011, **4**, 1781–1781.
58. H. Ye, H. S. Park and A. J. Bard, *J. Phys. Chem. C*, 2011, **115**, 12464–12470.
59. S. K. Pilli, T. E. Furtak, L. D. Brown, T. G. Deutsch, J. A. Turner and A. M. Herring, *Energy Environ. Sci.*, 2011, **4**, 5028–5028.
60. D. K. Zhong, S. Choi and D. R. Gamelin, *J. Am. Chem. Soc.*, 2011, **133**, 18370–18377.

61. J. A. Seabold and K.-S. Choi, *J. Am. Chem. Soc.*, 2012, **134**, 2186–2192.
62. W. J. Youngblood, S-H. A. Lee, K. Maeda and T. E. Mallouk, *Acc. Chem. Res.*, 2009, **42**, 1966–1973.
63. C. Xiang, G. M. Kimball, R. L. Grimm, B. S. Brunschwig, H. A. Atwater and N. S. Lewis, *Energy Environ. Sci.*, 2011, **4**, 1311–1311.
64. A. Paracchino, V. Laporte, K. Sivula, M. Grätzel and E. Thimsen, *Nat. Mater.*, 2011, **10**, 456–461.
65. C. M. McShane and K.-S. Choi, *J. Am. Chem. Soc.*, 2009, **131**, 2561–2569.
66. E. C. Garnett, M. L. Brongersma, Y. Cui and M. D. McGehee, *Annu. Rev. Mater. Res.*, 2011, **41**, 269–295.
67. A. I. Hochbaum and P. Yang, *Chem. Rev.*, 2010, **110**, 527–546.
68. X. Liu, Y. Z. Long, L. Liao, X. Duan and Z. Fan, *ACS Nano*, 2012, **6**, 1888–1900.
69. W. Lu and C. M. Lieber, *J. Phys. D: Appl. Phys.*, 2006, **39**, R387–R406.
70. W. Lu and C. M. Lieber, *Nat. Mater.*, 2007, **6**, 841–850.
71. P. J. Pauzauskie and P. Yang, *Mater. Today*, 2006, **9**, 36–45.
72. M. Yu, Y.-Z. Long, B. Sun and Z. Fan, *Nanoscale*, 2012, **4**, 2783–2796.
73. Z. Huang, N. Geyer, P. Werner, J. de Boor and U. Gösele, *Adv. Mater.*, 2011, **23**, 285–308.
74. K. Peng, X. Wang and S.-T. Lee, *Appl. Phys. Lett.*, 2008, **92**, 163103–163103.
75. H. M. Branz, V. E. Yost, S. Ward, K. M. Jones, B. To and P. Stradins, *Appl. Phys. Lett.*, 2009, **94**, 231121–231121.
76. J. Oh, T. G. Deutsch, H.-C. Yuan and H. M. Branz, *Energy Environ. Sci.*, 2011, **4**, 1690–1690.
77. K-Q. Peng, X. Wang, X.-L. Wu and S.-T. Lee, *Nano Lett.*, 2009, **9**, 3704–3709.
78. X. Shen, B. Sun, F. Yan, J. Zhao, F. Zhang, S. Wang, X. Zhu and S. Lee, *ACS Nano*, 2010, **4**, 5869–5876.
79. Y. Hou, B. L. Abrams, P. C. K. Vesborg, M. E. Björketun, K. Herbst, L. Bech, A. M. Setti, C. D. Damsgaard, T. Pedersen, O. Hansen, J. Rossmeisl, S. Dahl, J. K. Nørskov and I. Chorkendorff, *Nat. Mater.*, 2011, **10**, 434–438.
80. R. S. Wagner and W. C. Ellis, *Appl. Phys. Lett.*, 1964, **4**, 89–89.
81. A. P. Goodey, S. M. Eichfeld, K.-K. Lew, J. M. Redwing and T. E. Mallouk, *J. Am. Chem. Soc.*, 2007, **129**, 12344–12345.
82. E. A. Santori, J. R. Maiolo Iii, M. J. Bierman, N. C. Strandwitz, M. D. Kelzenberg, B. S. Brunschwig, H. A. Atwater and N. S. Lewis, *Energy Environ. Sci.*, 2012, **5**, 6867–6867.
83. J. R. McKone, E. L. Warren, M. J. Bierman, S. W. Boettcher, B. S. Brunschwig, N. S. Lewis and H. B. Gray, *Energy Environ. Sci.*, 2011, **4**, 3573–3583.
84. G. Yuan, H. Zhao, X. Liu, Z. S. Hasanali, Y. Zou, A. Levine and D. Wang, *Angew. Chem., Int. Ed.*, 2009, **48**, 9680–9684.

85. K. E. Plass, M. A. Filler, J. M. Spurgeon, B. M. Kayes, S. Maldonado, B. S. Brunschwig, H. A. Atwater and N. S. Lewis, *Adv. Mater.*, 2009, **21**, 325–328.
86. J. M. Spurgeon, S. W. Boettcher, M. D. Kelzenberg, B. S. Brunschwig, H. A. Atwater and N. S. Lewis, *Adv. Mater.*, 2010, **91125**, 3277–3281.
87. J. M. Spurgeon, K. E. Plass, B. M. Kayes, B. S. Brunschwig, H. A. Atwater and N. S. Lewis, *Appl. Phys. Lett.*, 2008, **93**, 032112–032112.
88. S. L. McFarlane, B. A. Day, K. McEleney, M. S. Freund and N. S. Lewis, *Energy Environ. Sci.*, 2011, **4**, 1700–1700.
89. J. M. Spurgeon, M. G. Walter, J. Zhou, P. A. Kohl and N. S. Lewis, *Energy Environ. Sci.*, 2011, **4**, 1772–1772.
90. E. Aharon-Shalom and A. Heller, *J Electrochem. Soc.*, 1982, **129**, 2865–2865.
91. A. Heller, *Solar Energy*, 1982, **29**, 153–162.
92. A. Heller and R. G. Vadimsky, *Phys. Rev. Lett.*, 1981, **46**, 1153–1153.
93. B. H. Erne, D. Vanmaekelbergh and J. J. Kelly, *J. Electrochem. Soc.*, 1996, **143**, 305–314.
94. K. Hagedorn, S. Collins and S. Maldonado, *J. Electrochem. Soc.*, 2010, **157**, D588–D588.
95. M. J. Price and S. Maldonado, *J. Phys. Chem. C.*, 2009, **113**, 11988–11994.
96. O. Khaselev and J. A. Turner, *Science*, 1998, **280**, 425–427.
97. B. D. James, G. N. Baum, J. Perez and K. N. Baum, *Technoeconomic Analysis of Photoelectrochemical (PEC) Hydrogen Production,* GS-10F-009, U.S. DOE, 2009.
98. K. Maeda, K. Teramura, D. Lu, N. Saito, Y. Inoue and K. Domen, *J. Phys. Chem. C.*, 2007, **111**, 7554–7560.
99. M. Yoshida, K. Takanabe, K. Maeda, A. Ishikawa, J. Kubota, Y. Sakata, Y. Ikezawa and K. Domen, *J. Phys. Chem. C*, 2009, **113**, 10151–10157.
100. A. B. Laursen, S. Kegnæs, S. Dahl and I. Chorkendorff, *Energy Environ. Sci.*, 2012, **5**, 5577–5577.
101. V. Chandra Srivastava, *RSC Adv.*, 2012, **2**, 759–759.
102. B. Hinnemann, P. G. Moses, J. Bonde, K. P. Jorgensen, J. H. Nielsen, S. Horch, I. Chorkendorff and J. K. Norskov, *J. Am. Chem. Soc.*, 2005, **127**, 5308–5309.
103. T. F. Jaramillo, K. P. Jorgensen, J. Bonde, J. H. Nielsen, S. Horch and I. Chorkendorff, *Science*, 2007, **317**, 100–102.
104. J. Bonde, P. G. Moses, T. F. Jaramillo, J. K. Norskov and I. Chorkendorff, *Faraday Discuss.*, 2008, **140**, 219–231.
105. Y. Hou, B. L. Abrams, P. C. K. Vesborg, M. r. E. Björketun, K. Herbst, L. Bech, B. Seger, T. Pedersen, O. Hansen, J. Rossmeisl, S. r. Dahl, J. K. Nórskov and I. Chorkendorff, *J. Photonics Energy*, 2012, **2**, 026001–026001.
106. D. Merki, S. Fierro, H. Vrubel and X. Hu, *Chem. Sci.*, 2011, **2**, 1262–1262.
107. D. Merki, H. Vrubel, L. Rovelli, S. Fierro and X. Hu, *Chem. Sci.*, 2012, **3**, 2515–2525.

108. R. E. Rocheleau, E. L. Miller and A. Misra, *Energy Fuels*, 1998, **12**, 3–10.
109. D. E. Brown, M. N. Mahmood, A. K. Turner, S. M. Hall and P. O. Fogarty, *Int. J. Hydrogen Energy*, 1982, **7**, 405–410.
110. D. E. Brown, M. N. Mahmood, M. C. M. Man and A. K. Turner, *Electrochim. Acta*, 1984, **29**, 1551–1556.
111. S. Y. Reece, J. A. Hamel, K. Sung, T. D. Jarvi, A. J. Esswein, J. J. H. Pijpers and D. G. Nocera, *Science*, 2011, **334**, 645–648.
112. B. E. Conway, H. Angersteinkozlowska, M. A. Sattar and B. V. Tilak, *J. Electrochem. Soc.*, 1983, **130**, 1825–1836.
113. B. E. Conway and L. Bai, *J. Chem. Soc., Faraday Trans. I*, 1985, **81**, 1841–1862.
114. M. W. Kanan and D. G. Nocera, *Science*, 2008, **321**, 1072–1075.
115. B. Wakkad and A. Hickling, *Trans. Faraday. Soc.*, 1950, **46**, 820–824.
116. *United States Pat.*, 3,399, **966**, 1968.
117. C. Iwakura, A. Honji and H. Tamura, *Electrochim. Acta*, 1981, **26**, 1319–1326.
118. Y. Surendranath, M. Dincă and D. G. Nocera, *J. Am. Chem. Soc.*, 2009, **131**, 2615–2620.
119. E. R. Young, D. G. Nocera and V. Bulović, *Energy Environ. Sci.*, 2010, **3**, 1726–1726.
120. J. G. McAlpin, Y. Surendranath, M. Dincă, T. A. Stich, S. A. Stoian, W. H. Casey, D. G. Nocera and R. D. Britt, *J. Am. Chem. Soc.*, 2010, **132**, 6882–6883.
121. J. B. Gerken, J. G. McAlpin, J. Y. C. Chen, M. L. Rigsby, W. H. Casey, R. D. Britt and S. S. Stahl, *J. Am. Chem. Soc.*, 2011, **133**, 14431–14442.
122. A. J. Esswein, Y. Surendranath, S. Y. Reece and D. G. Nocera, *Energy Environ. Sci.*, 2011, **4**, 499–499.
123. J. J. H. Pijpers, M. T. Winkler, Y. Surendranath, T. Buonassisi and D. G. Nocera, *Proc. Natl. Acad. Sci. U.S.A.*, 2011, **108**, 10056–10061.
124. E. R. Young, R. Costi, S. Paydavosi, D. G. Nocera and V. Bulović, *Energy Environ. Sci.*, 2011, **4**, 2058–2058.
125. D. K. Zhong, M. Cornuz, K. Sivula, M. Grätzel and D. R. Gamelin, *Energy Environ. Sci.*, 2011, **4**, 1759–1759.
126. E. M. P. Steinmiller and K.-S. Choi, *Proc. Natl. Acad. Sci. U.S.A.*, 2009, **106**, 20633–20636.
127. K. J. McDonald and K.-S. Choi, *Chem. Mater.*, 2011, **23**, 1686–1693.
128. T. Nakagawa, C. A. Beasley and R. W. Murray, *J. Phys. Chem. C*, 2009, **113**, 12958–12961.
129. Y. Zhao, N. M. Vargas-Barbosa, E. A. Hernandez-Pagan and T. E. Mallouk, *Small*, 2011, **7**, 2087–2093.
130. H. J. Lewerenz, *J. Electroanal. Chem.*, 2011, **662**, 184–195.
131. Y. W. Chen, J. D. Prange, S. Dühnen, Y. Park, M. Gunji, C. E. D. Chidsey and P. C. McIntyre, *Nature Mat.*, 2011, **10**, 539–544.
132. L. A. Kibler, *ChemPhysChem*, 2006, **7**, 985–991.
133. J. K. Nørskov, T. Bligaard, J. Rossmeisl and C. H. Christensen, *Nat. Chem.*, 2009, **1**, 37–46.

134. M. E. Björketun, A. S. Bondarenko, B. L. Abrams, I. Chorkendorff and J. Rossmeisl, *Phys. Chem. Chem. Phys.*, 2010, **12**, 10536–10541.
135. J. Greeley, T. F. Jaramillo, J. Bonde, I. Chorkendorff and J. K. Norskov, *Nat. Mater.*, 2006, **5**, 909–913.
136. J. Rossmeisl, A. Logadottir and J. K. Nørskov, *Chem. Phys.*, 2005, **319**, 178–184.
137. J. Rossmeisl, Z. W. Qu, H. Zhu, G. J. Kroes and J. K. Nørskov, *J. Electroanal. Chem.*, 2007, **607**, 83–89.